agronomy

MDPI

Article

An Analysis of Spatial–Temporal Evolution and Propagation Features of Vegetation Drought in Different Sub-Zones of China

Shikai Gao [1], Hexin Lai [1], Fei Wang [1,*], Xiaoman Qiang [2], Hao Li [2] and Danyang Di [3]

[1] School of Water Conservancy, North China University of Water Resources and Electric Power, Zhengzhou 450046, China; igaoshikai@163.com (S.G.); laihexin0214@126.com (H.L.)
[2] Key Laboratory of Crop Water Use and Regulation of Ministry of Agriculture and Rural Affairs, Farmland Irrigation Research Institute, Chinese Academy of Agriculture Sciences, Xinxiang 453003, China; xiaomanqiang@caas.cn (X.Q.); lihao01@caas.cn (H.L.)
[3] School of Water Conservancy and Transportation, Zhengzhou University, Zhengzhou 450001, China; danyangdi@zzu.edu.cn
* Correspondence: wangfei@ncwu.edu.cn; Tel.: +86-1-823-692-7593

Abstract: The vegetation drought phenomenon will reduce the amount of water available to the vegetation system, change the ecological and hydrological cycles of plants, and affect the aquatic and terrestrial ecosystem in various forms. Therefore, research on the dynamic variation and driving mechanism of vegetation drought will help us recognize and predict the response of vegetation under drought stress conditions, implement appropriate policy measures to deal with the drought crisis, and provide technical support for implementing vegetation protection and alleviating the increasing risk of vegetation drought. However, the dynamic variation of vegetation drought and its dynamic propagation mechanism are still undefined across China. In this study, the spatio-temporal evolutions and pixel-scaled trends of vegetation drought were analyzed during the period between 1999 and 2020. Additionally, the propagation features were investigated between vegetation drought and meteorological drought. Finally, the relationships between vegetation drought and atmospheric teleconnection were explicitly clarified using multivariate cross wavelet transform technology. The results highlighted five key findings: (1) the vegetation drought presented an overall decreasing trend across China in 1999–2020; (2) the most serious vegetation drought occurred in the year 2000, with the average vegetation condition index (VCI) values ranging from 0.36 to 0.46; (3) vegetation droughts were alleviating at the pixel scale for each season; (4) the propagation time from meteorological drought to vegetation drought was shorter in summer (1.26 months) and longer in winter (2.26 months); and (5) the three-factors combination of Pacific North American (PNA), El Niño-Southern Oscillation (ENSO), and Trans Polar Index (TPI) can satisfactorily explain the variations of vegetation drought. This study sheds new viewpoints into the identification of vegetation drought variation across China, which can also be applied in other areas.

Keywords: vegetation drought; dynamic variations; atmospheric teleconnection; multivariate cross wavelet transform technology; China

Citation: Gao, S.; Lai, H.; Wang, F.; Qiang, X.; Li, H.; Di, D. An Analysis of Spatial–Temporal Evolution and Propagation Features of Vegetation Drought in Different Sub-Zones of China. *Agronomy* **2023**, *13*, 2101. https://doi.org/10.3390/agronomy13082101

Received: 15 June 2023
Revised: 5 August 2023
Accepted: 7 August 2023
Published: 10 August 2023

1. Introduction

Droughts are defined as complex phenomena with continuous and abnormal precipitation deficits, which can be divided into four categories, i.e., meteorological drought, agricultural drought, hydrological drought, and socio-economic drought [1–3]. Recently, vegetation drought has been defined as the inability of plants to absorb sufficient water to meet their requirements, which will lead to a change in the terrestrial vegetation growth state and soil moisture condition and will place multiple pressures on the ecological environment [4]. Crausbay et al. further proposed a framework for vegetation drought, which was composed of several components, i.e., exposure, sensibility, and fragility [5]. In addition, the enhancement of anthropogenic water demand reduces the available water in the vegetation ecosystem, changes the hydrological and ecological process, and affects the aquatic and terrestrial ecosystem in various ways. Traditional drought indicators rarely focus on the response of surface vegetation to a drought process, and have different performances in ecological, hydrological, and vegetational drought monitoring [6,7]. Based on the spectral reflection information of ground objects, the remotely sensed drought indicators can reflect the vegetation structure under drought circumstances and are practical for large-scale vegetation drought monitoring [8–12].

For aquatic ecosystems, McEvoy et al. analyzed five drought planning measures at the basin scale in southwestern Montana using a vegetation drought framework, in order to estimate the ecological effects of drought [13]. For terrestrial ecosystems, a remotely sensed vegetation index is usually employed to portray the status of vegetation under drought stress, with simple, effective, and empirical measurement of terrestrial vegetation and ecological conditions [14–16]. Remote sensing satellites can provide valuable information for drought monitoring in visible, near-infrared, thermal-infrared, and other bands. Additionally, vegetation dynamic change monitoring based on the vegetation index is used to identify the internal and external state changes of plants by using the different spectral characteristics reflected by the calibrated remote sensing images in different periods [17,18]. As one of the sensitive indicators of global eco-environmental change, vegetation growth signal plays an important role in environmental change detection, ecosystem maintenance, and agricultural production guidance [19–21]. Under drought stress, the changes in vegetation apparent characteristics and growth activity will cause significant changes in vegetation reflectance in different spectral bands [22]. The dynamic monitoring of vegetation can reflect the ecosystem change trend. Therefore, monitoring the dynamic change of vegetation and analyzing the relationship between this change and the terrestrial ecosystem has become an important field of global drought change research [23–26].

In the 21st century, droughts have characteristics of long duration, wide coverage, and serious detriment, increasing the vulnerability of vegetation ecosystem [27,28]. In the past, people mostly focused on the hydrological, agricultural, and socio-economic impact of drought, and paid less attention to its impact on vegetation growth status. More recently, with the aggravation of drought frequency and intensity, and the increase in adverse drought effects on vegetation and the ecosystem, more ecologists began to focus on the ecological aspects within vegetation drought [29,30]. For example, the severe drought in Australia from 2002 to 2010, as strong as the 1000-year event, caused vegetation losses of more than 800 million dollars in the ecosystem over the Murray–Darling region [31]. From the 21st century, droughts have brought about vegetation degradation and ecological environment deterioration in the Qilian Mountains [32]. Frequent droughts lead to vegetation losses at different levels and hinder flourishing growth of vegetation, accompanied by different drought trigger thresholds in eight divisions of vegetation across China [33]. Thus, vegetation drought investigation is an effective and important means of controlling ecological degradation, restoring ecosystem function, and improving environment quality.

Drought propagation is a dynamic evolution process of water deficit in the time dimension, which involves water deficiency in any procedure of the hydrologic cycle [34]. The meteorological drought that mainly manifests through insufficient precipitation is generally the first phase of rapid development of drought, and it will cause a reduction in crop yield [35]. Additionally, long-term precipitation deficit will arouse surface water drought and groundwater drought, which has properties in the lack of supplement of surface or underground runoff [36,37]. In the study of drought transmission, the propagation time between meteorological drought and hydrological drought is shorter in spring and summer than that in autumn and winter, with obvious seasonal characteristics [38]. The propagation time was shorter in the sub-basin dominated by grassland (1–5 months) than in the sub-basin dominated by forest (4–7 months) in northern China [39]. The propagation of agricultural drought was slow in autumn and relatively fast in summer [40]. Existing studies mainly focus on the propagation dynamics between meteorological drought and hydrological drought, while paying less attention to the mechanism of meteorological drought driving vegetation drought. Generally, it is difficult for humans to affect rainfall patterns, but we can adjust water and soil resources management strategies to alleviate or reduce drought losses by clarifying the complex responses between vegetation drought and meteorological drought. Furthermore, relevant investigations [41–44] have demonstrated that the large-scale circumfluence factors played important roles in the occurrence of drought. However, the relationship between vegetation drought and atmospheric teleconnections has not been reported yet on a national scale.

Therefore, this study aims to (1) identify the temporal variations and spatial distributions of vegetation drought; (2) investigate the pixel-scaled vegetation drought trends; (3) reveal the propagation dynamics from meteorological drought to vegetation drought; and (4) determine the dynamic relations between vegetation drought and atmospheric teleconnections.

2. Study Area and Dataset

2.1. Study Area

China is located in the southeast of the Eurasian continent, bordering the Pacific Ocean in the East. Western China is dominated by plateaus, mountains, and the Tarim basin, and eastern China is dominated by plains and hills. On the whole, the annual precipitation exhibits a gradient trend from the southeast coast to the northwest inland, accompanied by more precipitation in coastal areas and southern areas. The vegetation and ecological environment have a strong regional conjugation and dynamic stability in China. Therefore, strengthening the investigation of vegetation drought is conducive to controlling ecological degradation, restoring ecosystem function, improving ecological environment quality, and ultimately maintaining the integrity of the ecosystem and realizing the harmonious development of humans and nature. On account of regional vegetation types, there are eight major vegetation sub-zones across China (Figure 1). The detailed sub-zones are listed in Table 1.

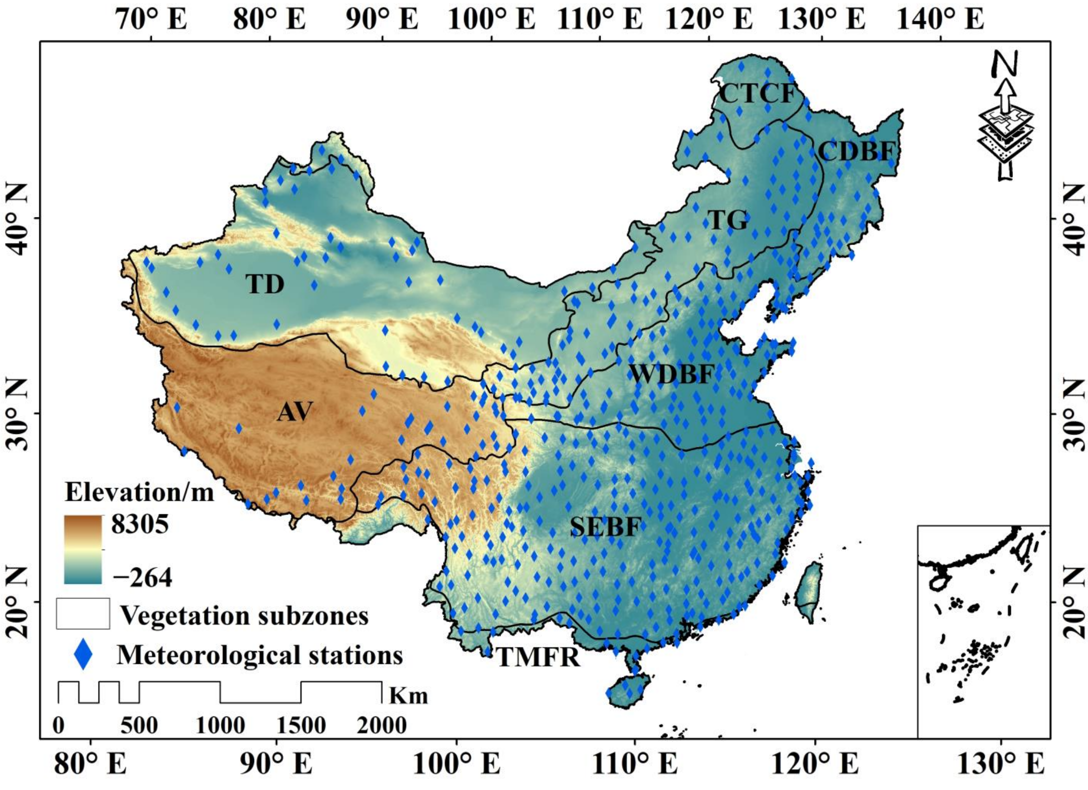

Figure 1. Vegetation sub-zones and meteorological stations located in China.

Table 1. List of regions in this study.

Region	Abbreviation	Area (10^4 km^2)	Number of Meteorological Stations
Temperate Desert	TD	218.06	47
Temperate Grassland	TG	116.41	87
Alpine Vegetation	AV	160.59	34
Subtropical Evergreen Broad-leaved Forest	SEBF	267.08	259
Tropical Monsoon Forest and Rainforest	TMFR	28.96	19
Warm-Temperate Deciduous Broad-leaved Forest	WDBF	97.07	120
Coniferous and Deciduous Broad-leaved Forest	CDBF	40.84	35
Cold-Temperate Coniferous Forest	CTCF	20.79	6
Mainland China	MC	949.80	607

2.2. Dataset

2.2.1. In Situ Data

The in situ data were derived from a surface climatic monthly dataset for 613 meteorological stations covering 1960–2020, including the monthly precipitation, average temperature, extreme temperature, vapor pressure, average wind speed, and sunlight duration (http://data.cma.cn (accessed on 6 March 2022)). Through strict extreme value tests, homogeneity tests and screening, we selected 607 meteorological stations data that met the quality requirements.

2.2.2. Remote Sensing Satellite Dataset

The Normalized Difference Vegetation Index (NDVI) dataset was obtained from SPOT/VEGETATION satellite during 1999–2020 (1 km resolution), and has been re-processed by means of radiometric calibration, geometric rectification, and noise reduction. As a distinctive spectral signal extracted by using the optical parameters of the leaf crown, NDVI is a powerful and dimensionless vegetation metric suitable for multiple biological populations and the fields related to vegetation dynamic variation, vegetation cover classification, and macro ecological aspects [16,45–47].

2.2.3. Atmospheric Teleconnection

Large-scale circumfluence indices were selected covering 1999–2020, i.e., El Niño-Southern Oscillation (ENSO), Arctic Oscillation (AO), Southern Oscillation Index (SOI), Pacific North American (PNA), Sunspot Index (SI), Dipole Mode Index (DMI), Trans Polar Index (TPI), and North Pacific Index (NPI) (https://psl.noaa.gov/data/climateindices/list/) (accessed on 5 December 2021). The atmospheric teleconnections used in this study are listed in Table 2.

Table 2. The atmospheric teleconnections used in this study.

Atmospheric Teleconnections	Acronym	Period
El Niño-Southern Oscillation	ENSO	1999–2020
Arctic Oscillation	AO	1999–2020
Southern Oscillation Index	SOI	1999–2020
Pacific North American	PNA	1999–2020
Sunspot Index	SI	1999–2020
Dipole Mode Index	DMI	1999–2020
Trans Polar Index	TPI	1999–2020
North Pacific Index	NPI	1999–2020

2.2.4. Digital Elevation Model Data

The spatial distribution of elevation was derived from the Shuttle Radar Topography Mission (SRTM) dataset in the American space shuttle Endeavour. The dataset is generated using WGS84 ellipsoidal projection and resampled based on the latest SRTM V4.1 data, which has a strength of strong reality and free access and is used for ecological environment analysis [48].

3. Methodology

3.1. Vegetation Condition Index

VCI can reflect an arid ecological environment formed by the interaction between vegetation and its living environment, and has a good representational ability for the physiological response of vegetation under drought stress [10,49]. Additionally, VCI is a reliable measurement of vegetation coverage and crop growth status in the terrestrial areas, which can reflect the fluctuation of ecosystem productivity caused by differences in meteorological conditions. Meanwhile, VCI is sensitive to drought stress and can weaken or even eliminate the impact on vegetation due to different geographical location, ecosystem, and soil conditions [11]. In this study, in order to quantitatively evaluate the applicability of VCI across China, the calculated VCI (VCI_s) from the SPOT/VEGETATION satellite was compared with the VCI product (VCI_p) from the Advanced Very-High-Resolution Radiometer (AVHRR). Four evaluation indicators were used to validate VCI, including Correlation Coefficient (r), Root Mean Square Error (RMSE), Mean Absolute Error (MAE), and Nash–Sutcliffe Efficiency (NSE).

The VCI and evaluation indicator calculation is as follows:

$$\mathrm{VCI} = \frac{NDVI_i - NDVI_{\mathrm{min}}}{NDVI_{max} - NDVI_{min}} \tag{1}$$

$$\mathrm{r} = \frac{\sum_{i=1}^{n} (C_i - \overline{C})(H_i - \overline{H})}{\sqrt{\sum_{i=1}^{n} (C_i - \overline{C})^2}\sqrt{\sum_{i=1}^{n} (H_i - \overline{H})^2}} \tag{2}$$

$$\mathrm{RMSE} = \sqrt{\frac{1}{n}\sum_{i=1}^{n} (C_i - H_i)^2} \tag{3}$$

$$\mathrm{MAE} = \frac{1}{n}\sum_{i=1}^{n} |C_i - H_i| \tag{4}$$

$$\mathrm{NSE} = 1 - \frac{\sum_{i=1}^{n} (C_i - H_i)^2}{\sum_{i=1}^{n} (H_i - \overline{H})^2} \tag{5}$$

where C_i and H_i represent the VCI_s and VCI_p, $\overline{C}$ and $\overline{H}$ represent the mean values of VCI_s and VCI_p, and n represents the number of samples.

3.2. Meteorological Drought Index

The standardized precipitation evapotranspiration index (SPEI) is a robust meteorological drought index in light of multi-time scale and spatial comparability, which has the advantages of simple and convenient calculation, sensitive drought response, and flexible time scale [50,51]. The regional potential evapotranspiration is calculated on the basis of the meteorological data for multiple years with long sequences, and then the SPEI values are obtained based on the probability distribution of water loss time series.

3.3. Extreme-Point Symmetric Mode Decomposition (ESMD)

ESMD method can progressively decompose and identify large-scale circulation and non-linear trends of time series [52]. With the advantages of local signal variation and adaptability, ESMD optimizes the last residual component into a series of extreme points and diminishes the problems of complex screening times and rough trend function. More descriptions of the ESMD method can be found in [52].

3.4. Pixel-Scaled Trend Analysis Method

The nonparametric Mann–Kendall method is often used to diagnose the trend changes of precipitation, runoff, temperature, and other time series. However, the trend item is often disturbed due to the significant high-order autocorrelation component in the original sequence. The pixel-scaled Mann–Kendall (PMK) compresses the trend characteristic value of the spatio-temporal matrix into a graph and finally obtains the spatial variation trend. More procedures about the PMK method are referred to in [37].

3.5. Rescaled Range (R/S) Analysis

The R/S diagnostic method is usually used to investigate fractal characteristics and long-term memory processes within the time series [19,53]. During the R/S analysis, the Hurst index is used to predict future trends, which can reflect extended the persistence characteristics and memory degree of time series. The procedures applying the R/S analysis can be found in [19].

3.6. Bivariate and Multivariate Cross Wavelet Transform Technology

Bivariate cross wavelet transform can explain the similarity of periodic characteristics between two variables, while multivariate wavelet can describe the common characteristics within multiple variables [54–56]. Wavelet coherence can not only provide a spectrogram similar to Fourier analysis, but also capture the interaction between signals, which can reflect the local correlation in the time–frequency range. In addition, cross wavelet transform is a beneficial instrument used to detect the instantaneous coherence variation by obtaining the amplitude and phase information of a signal [55].

4. Results

4.1. The Validation of VCI

In order to quantitatively evaluate the performance of VCI across China, the evaluation indicators r, RMSE, MAE, and NSE were used to validate VCI (Figure 2). After calculation, the average r value was 0.62 in China, and the r value in the TG (0.66) and WDBF (0.67) was higher than 0.60. The average RMSE value was 0.27, with a relatively high RMSE value (0.31) in the TD. Similarly, the average MAE value was 0.22, with a high MAE value (0.25) in the TD. For the NSE, the average NSE value was 0.60 in China, and the higher NSE values occurred in the WDBF (0.72) and TG (0.70). Overall, VCI showed good consistency across China, implying that it is suitable for vegetation drought assessment.

4.2. Temporal Variations of Vegetation Drought

Figure 3 shows the eigenmode function component (EFC) and a trend item (TI) of VCI from 1999 to 2020 based on ESMD. When the optimal screening times reached 40 times, the TI could represent an overall fluctuation of the original VCI sequence. Furthermore, the contributions of variance in EFC1, EFC2, and TI were 48.18%, 6.87%, and 44.95%, respectively, suggesting that the EFC1 contributed to most variations in vegetation drought in China. On an inter-annual scale, vegetation drought has a 7-year period that can be reflected by EFC1. On an inter-decadal scale, a 10.5-year period can be obtained from EFC2. As shown in Figure 3, the original VCI sequence and trend component TI showed a consistent tendency of rising first and then falling during 1999–2020, and reached the minimum value (0.41) in 2000 and the maximum value (0.64) in 2013, respectively. Additionally, based on R/S analysis, the Hurst index was 0.60 (>0.50) in VCI time series, indicating a consistent trend between future and previous droughts. The VCI linear tendency rate was 0.044/10a with a minimum of 0.41 occurring in 2000, indicating that vegetation drought was generally decreasing from 1999 to 2020.

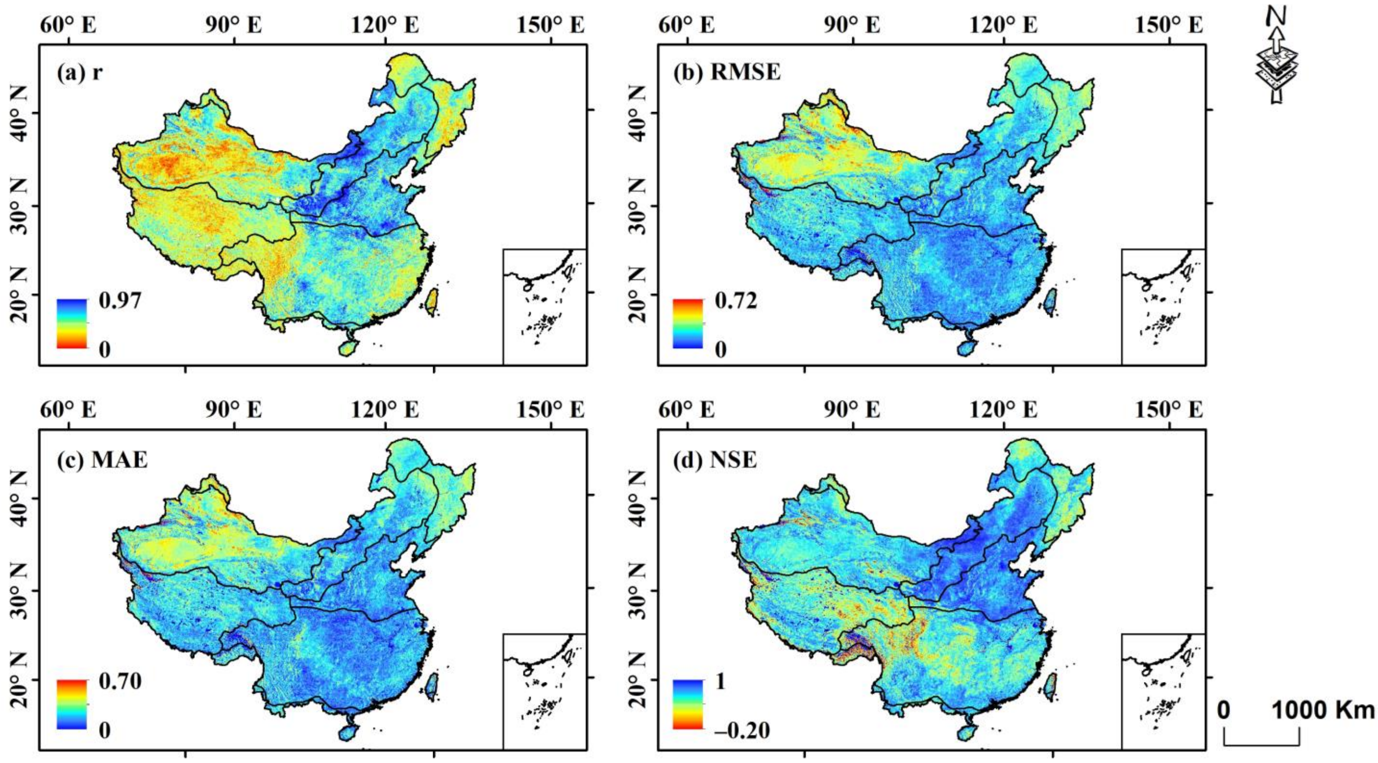

Figure 2. Spatial distribution of (**a**) r, (**b**) RMSE, (**c**) MAE, and (**d**) NSE across China.

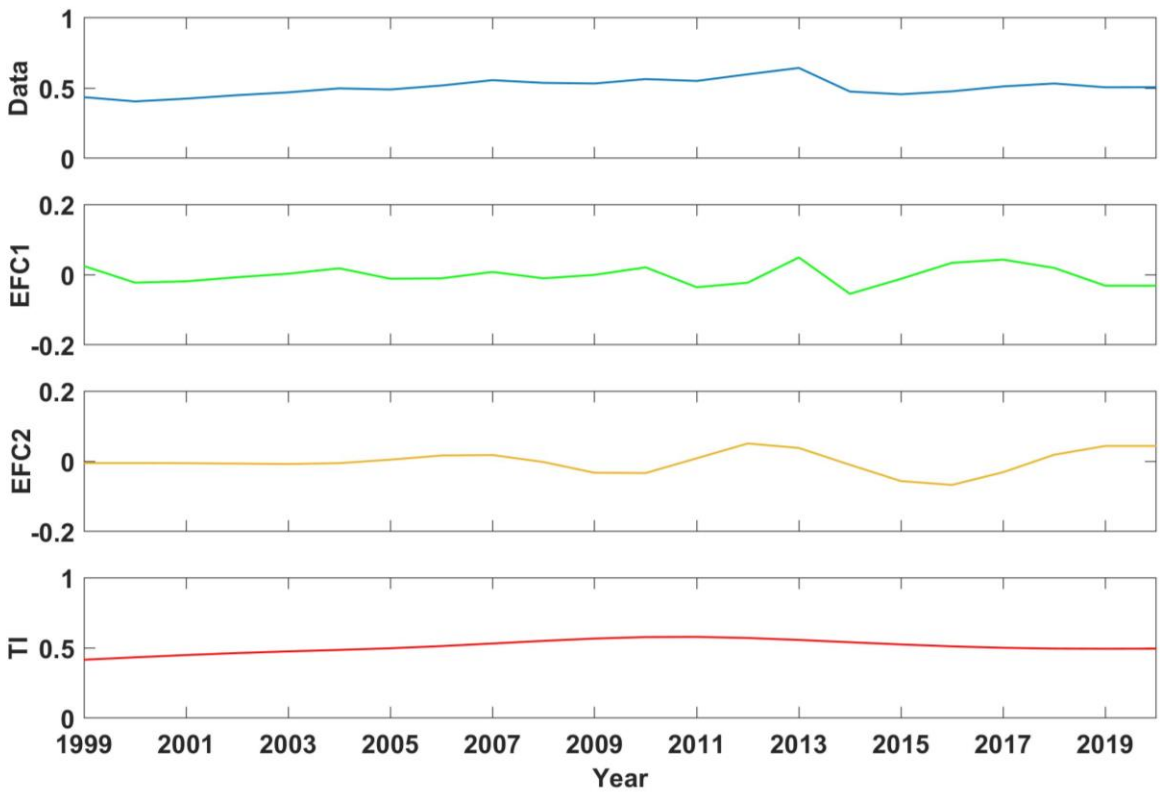

Figure 3. Two EFCs and a trend item TI of VCI during 1999–2020 based on ESMD.

Figure 4 indicates the temporal variations of VCI in various regions across China. The solid blue line represents the trend component TI obtained via ESMD time-frequency decomposition, and the dashed red line denotes the linear trend of the VCI time series.

During 1999–2020, the variation characteristics of VCI were different in each sub-region. Among them, the VCI manifested a downward trend in the TD and AV, indicating an increase in drought trend within these two sub-regions. Conversely, the VCI showed a significant upward trend, demonstrating that drought was significantly decreasing in the TG, SEBF, TMFR, WDBF, CDBF, and CTCF. In each sub-region, the most obvious upward trend appeared in the SEBF, with a 0.137/10a linear tendency rate of VCI, followed by the TMFR with a 0.129/10a linear tendency rate of VCI. Additionally, a severe drought emerged in the year 2000 in the TG, SEBF, TMFR, WDBF, CDBF, and CTCF, with a mean VCI-value of 0.35, 0.37, 0.38, 0.34, 0.34, and 0.32, respectively. Severe drought occurred in 2015 in the TD and AV, with a mean VCI-value of 0.25 and 0.35, respectively.

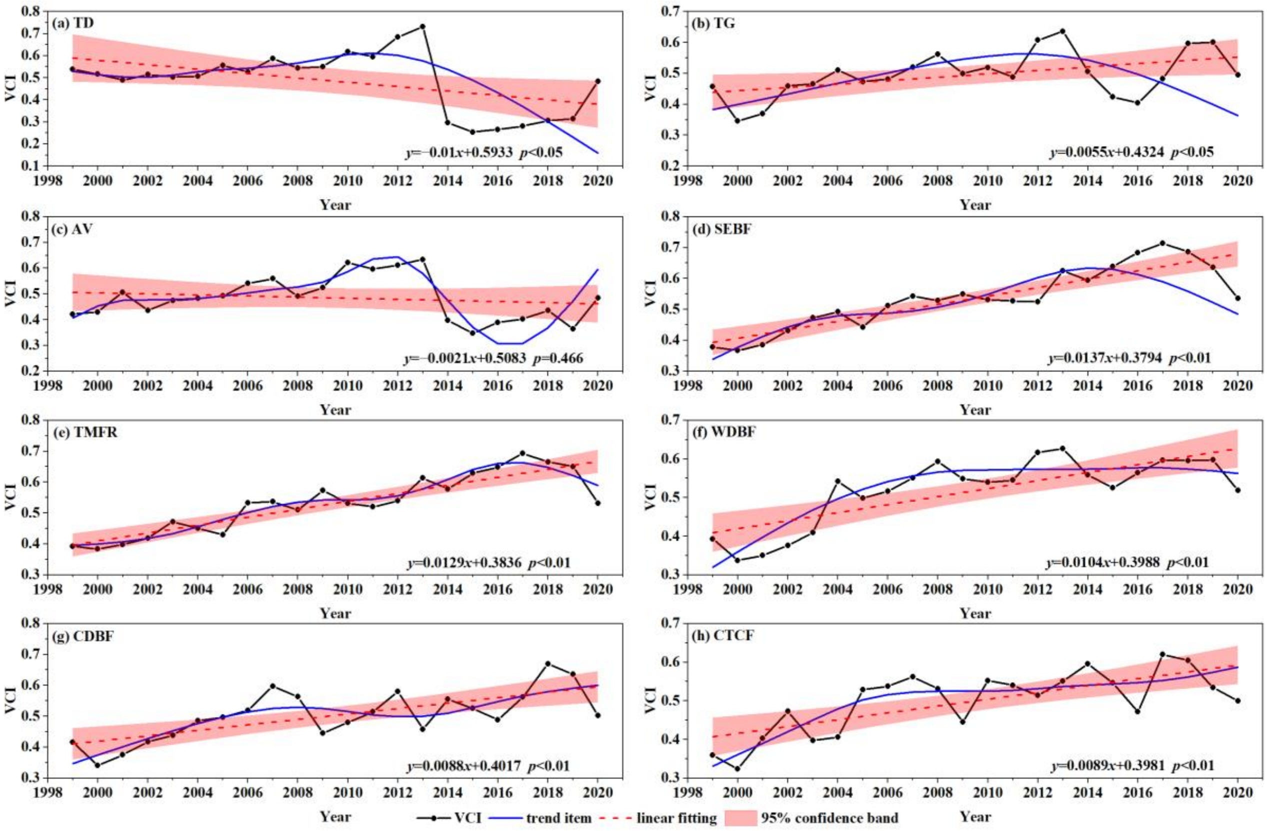

Figure 4. Temporal variations of VCI during 1999–2020 in each region (**a**) TD, (**b**) TG, (**c**) AV, (**d**) SEBF, (**e**) TMFR, (**f**) WDBF, (**g**) CDBF, and (**h**) CTCF.

4.3. Spatial Distributions of Vegetation Drought

Since the minimum VCI appeared in 2000 during 1999–2020, we selected 2000 as a typical drought year to explore the spatial patterns of vegetation drought in China (Figure 5). From a monthly scale perspective, the minimum and maximum VCI appeared in August (0.36) and November (0.46), respectively (Table 3). From a seasonal-scale perspective, the minimum and maximum VCI occurred in summer (0.40) and winter (0.44), respectively. In summer and autumn, droughts were mainly concentrated in the CTCF, with a mean VCI-value of 0.25, and 0.33, respectively. Moreover, spring drought was mainly concentrated in the SEBF, with a mean VCI-value of 0.34, and winter drought was mainly concentrated in the CDBF, with a mean VCI-value of 0.28.

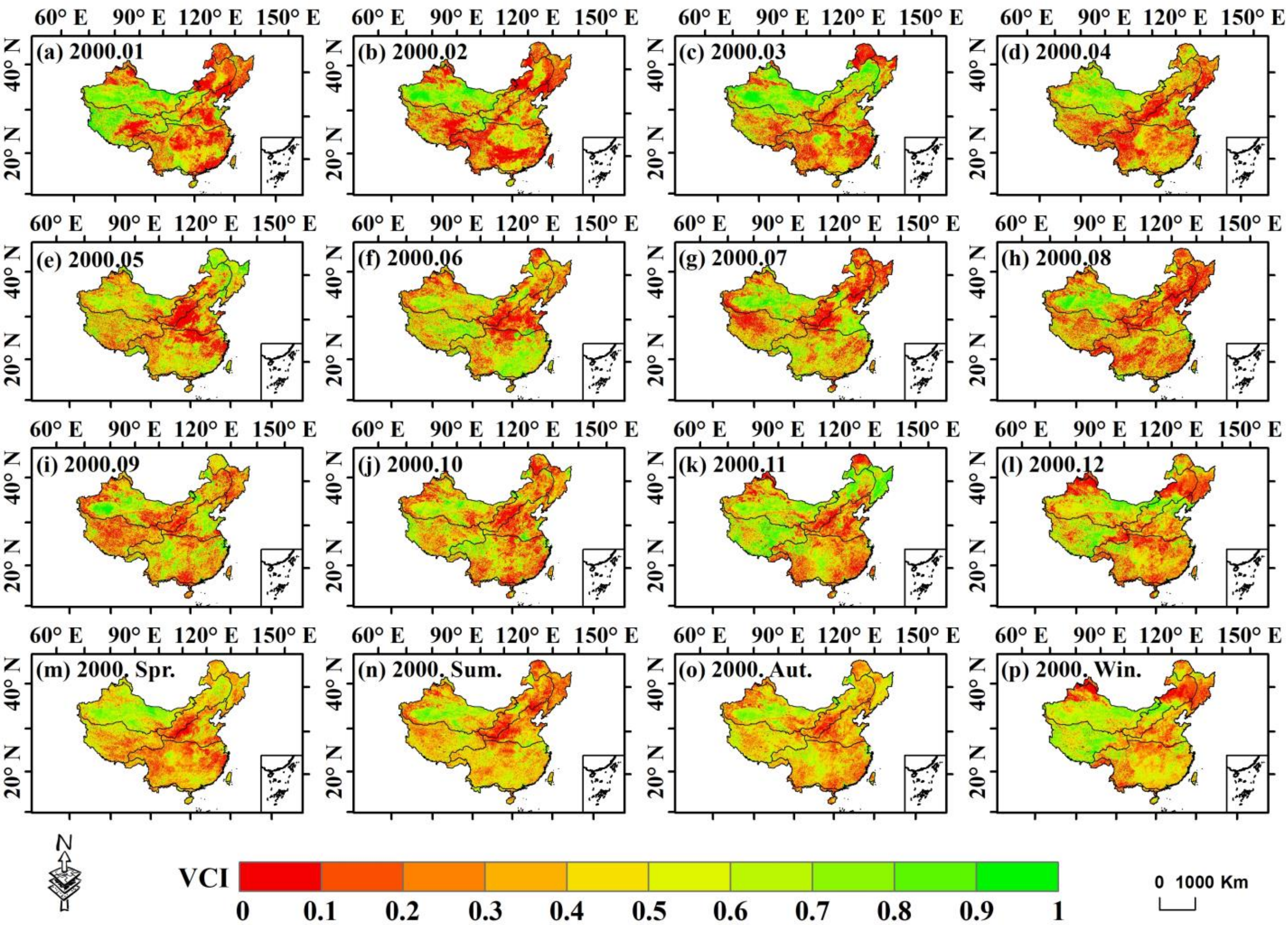

Figure 5. Spatial patterns of vegetation drought during 2000 in (**a**) January, (**b**) February, (**c**) March (**d**) April, (**e**) May, (**f**) June, (**g**) July, (**h**) August, (**i**) September, (**j**) October, (**k**) November, (**l**) December, (**m**) Spring, (**n**) Summer, (**o**) August, and (**p**) Winter across China.

Table 3. The minimum, maximum and mean VCI values in the year 2000.

VCI Value	Jan.	Feb.	Mar.	Apr.	May.	Jun.	Jul.	Aug.	Sep.	Oct.	Nov.	Dec.	Spr.	Sum.	Aut.	Win.
Min.	0.22	0.22	0.27	0.25	0.13	0.16	0.23	0.18	0.32	0.21	0.26	0.30	0.22	0.22	0.27	0.27
Max.	0.50	0.48	0.57	0.51	0.56	0.56	0.48	0.41	0.50	0.50	0.57	0.48	0.51	0.44	0.49	0.55
Mean	0.41	0.37	0.44	0.39	0.41	0.43	0.40	0.36	0.40	0.39	0.46	0.40	0.41	0.40	0.42	0.44

Figure 6 illustrates the spatial patterns of vegetation drought in different months and seasons across China. For all VCI pixels, the average VCI ranged from 0.49 (April) to 0.52 (November). Additionally, from a monthly scale perspective, the minimum VCI-values occurred in the CDBF (0.38), CDBF (0.38), CTCF (0.38), CDBF (0.39), CDBF (0.44), AV (0.44), CTCF (0.44), AV (0.45), AV (0.45), TD (0.45), AV (0.46), and CTCF (0.46) for January, February, March, December, April, May, October, June, July, August, September, and November, respectively (Figure 6a–l). Generally, from spring to summer, the average VCI gradually improved from 0.50 to 0.51. Then, the vegetation drought had an ascending intensity from summer to winter, with the average VCI decreasing from 0.51 to 0.49. In winter, summer, spring and autumn, the minimum VCI values occurred in the CDBF (0.38), AV (0.45), AV (0.47), and CTCF (0.49), respectively (Figure 6m–p). Apparently, the three vegetation-drought-prone areas were the CDBF, CTCF, and AV.

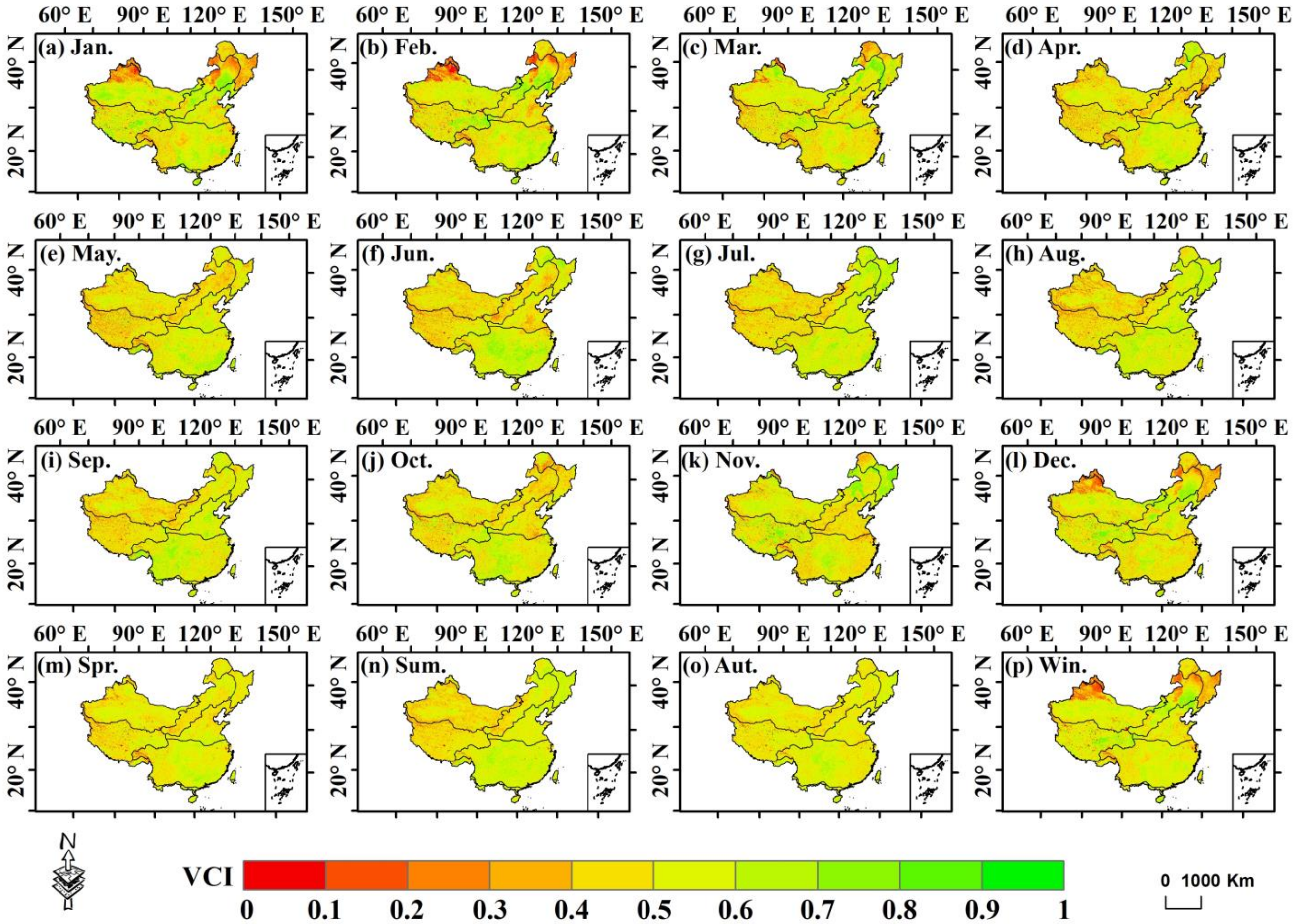

Figure 6. Spatial distribution of vegetation drought in different months (**a**) January, (**b**) February, (**c**) March (**d**) April, (**e**) May, (**f**) June, (**g**) July, (**h**) August, (**i**) September, (**j**) October, (**k**) November and seasons, (**l**) December, (**m**) Spring, (**n**) Summer, (**o**) August, and (**p**) Winter across China.

4.4. Vegetation Drought Trend Identification at the Pixel Scale

The pixel-scaled VCI trend characteristics are depicted in Figure 7. Figure 8 signifies the trend characteristic Z-values of VCI based on the PMK method across China from 1999 to 2020. From a monthly scale perspective, the average Z-values were −0.02 (January), –0.01 (February), 0.05 (March), 0.27 (April), 0.49 (May), 0.48 (June), 0.68 (July), 0.68 (August), 0.52 (September), 0.44 (October), 0.07 (November), and 0.02 (December), respectively (Figure 8). By and large, vegetation drought showed an increasing trend in January and February, and a decreasing trend from March to December. For all sub-regions, Z > 0 expressed an alleviating trend of vegetation drought in July and August. As Figure 9 shows, for the rising trend of drought, the percentage of area ranged from 30.7% (August) to 57.9% (December). Additionally, the maximum percentage of area (0.49%) was found in March (Figure 7), with an expanding trend of drought ($p < 0.01$). From a seasonal-scale perspective, the average Z-values were 0.41 (spring), 0.79 (summer), 0.50 (autumn), and 0.11 (winter), indicating that vegetation droughts were decreasing for each season across China (Figure 8). For all sub-regions except the TD, Z > 0 suggested a descending trend of vegetation drought in summer. In terms of the upward trend of drought, the percentage of area in each season was 44.3% (spring), 30.9% (summer), 39.1% (autumn), and 52.8% (winter), respectively. Furthermore, the maximum percentage of area (0.77%) was found in spring (Figure 7), with an expanding trend of drought ($p < 0.01$). In the CTCF, the alleviation trend of vegetation drought was observed in July at $p < 0.05$. In addition, the increasing vegetation drought mainly occurred in the TD, TG, and AV (Figure 8).

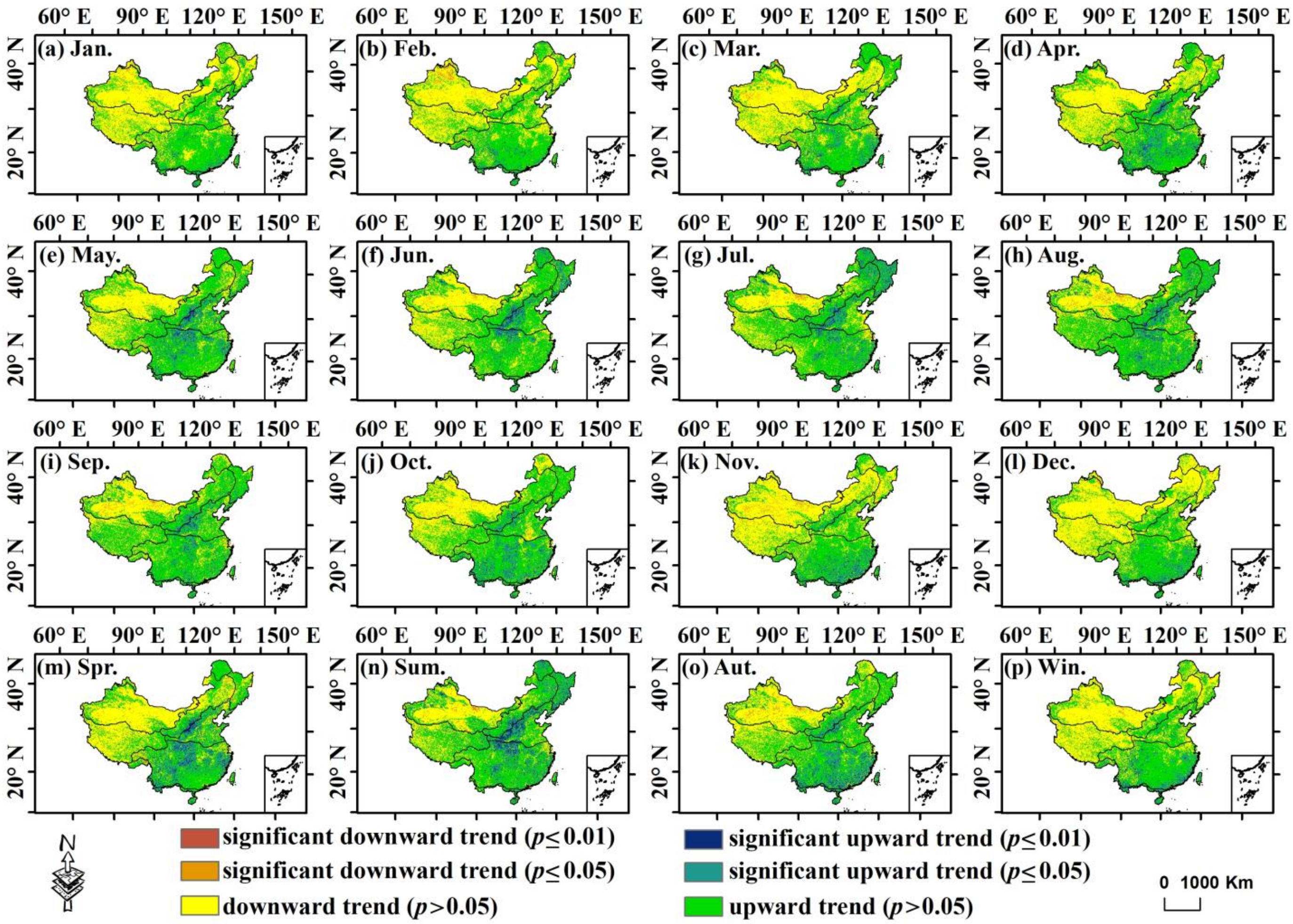

Figure 7. Pixel-scaled VCI trend identification in (**a**) January, (**b**) February, (**c**) March (**d**) April, (**e**) May, (**f**) June, (**g**) July, (**h**) August, (**i**) September, (**j**) October, (**k**) November, (**l**) December, (**m**) Spring, (**n**) Summer, (**o**) August, and (**p**) Winter across China during 1999–2020.

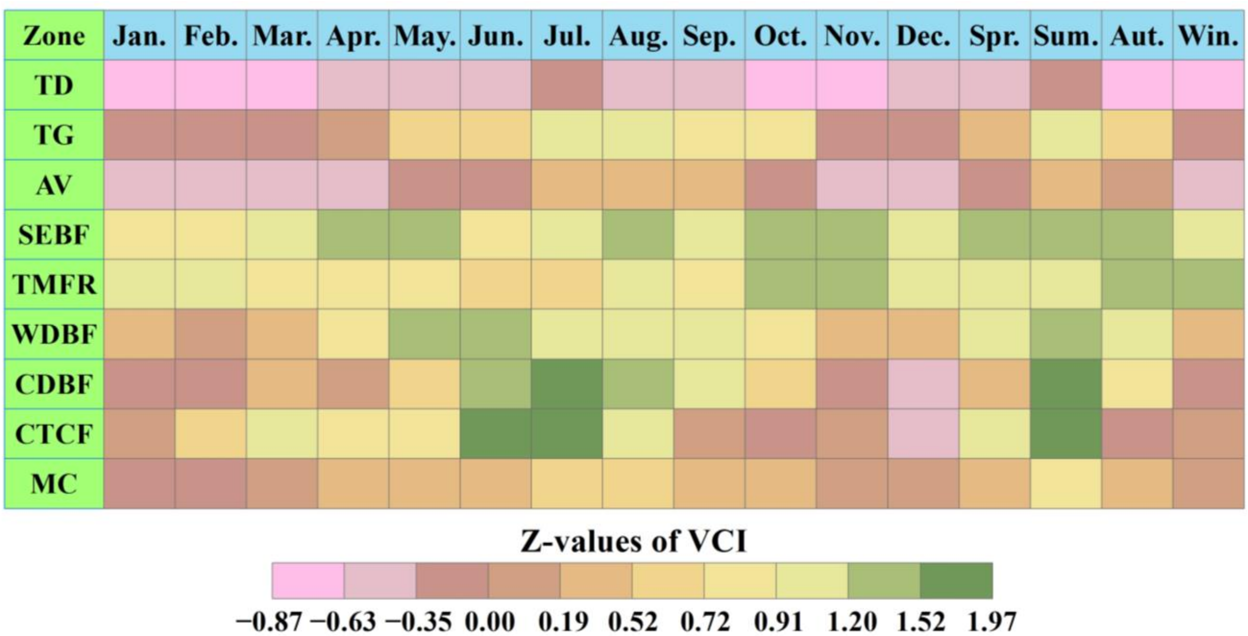

Figure 8. Z-values of VCI across China during 1999–2020.

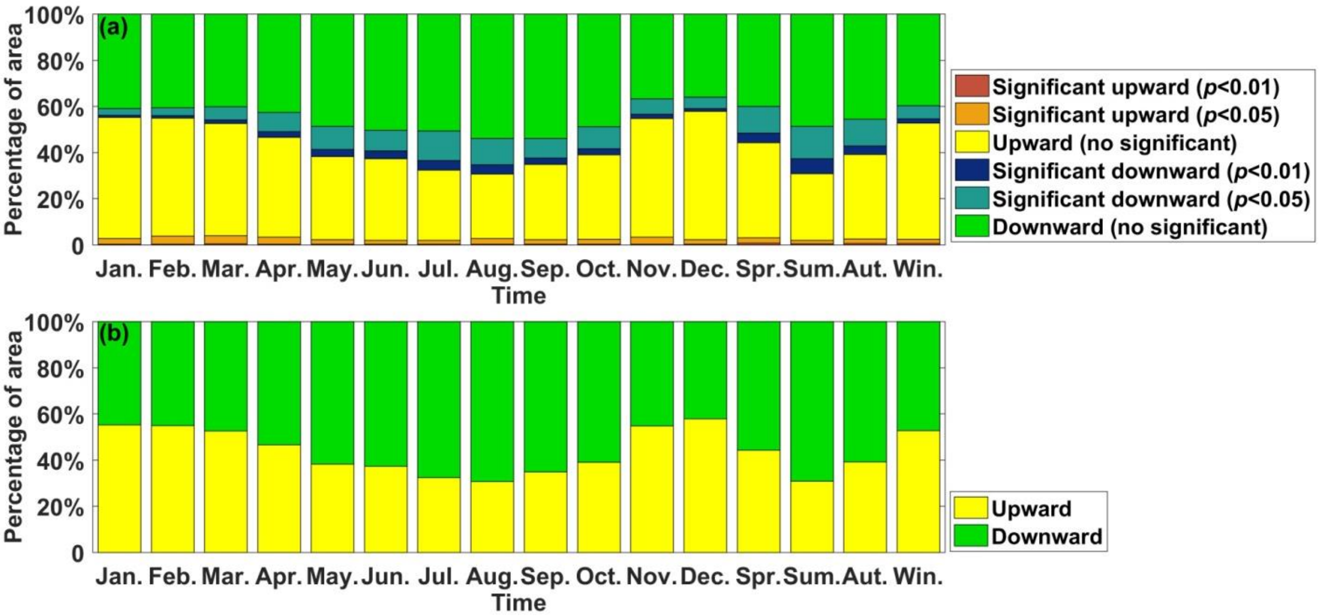

Figure 9. The percentage of area of vegetation drought trend divided into (**a**) six and (**b**) two categories in each month and season.

4.5. Propagation Features from Meteorological to Vegetation Drought

Since precipitation needs to be reflected in the growth of vegetation through slow soil infiltration and vegetation root absorption, the vegetation communities cannot respond to climate change instantaneously. In view of the response effects in vegetation drought and meteorological drought, it is necessary to investigate the propagation features from meteorological to vegetation drought. Previous studies demonstrated that the lag times of vegetation responses to climate were less than 3 months [6,8,21,45]. Accordingly, the r was calculated between the monthly VCI and the meteorological indicator SPEI (0–3-month scales) in each region of China (Figure 10). This study used the cross-correlation to analyze the hysteresis effect, and the lag time of vegetation drought to meteorological drought was determined [36,37,57]. In MC, the propagation time was 1—month in July (r = 0.65) and September (r = 0.42) and 0—month in August (0.70). Meanwhile, the propagation time was 2—month in January (r = 0.62), February (r = 0.53), April (r = 0.56), June (r = 0.69), October (r = 0.61), November (r = 0.67), and December (r = 0.74) and 3–month in March (r = 0.58) and May (r = 0.53), respectively. For the entire period, the number of 0—, 1—, 2— and 3—month propagation time was 7, 28, 46, and 27, respectively. Additionally, the ratio of r values was 89.81% and 58.33% at the significant level of 0.05 and 0.01. In summary, the time lag was shorter in summer (approximately 1.26 months) with an average r-value of 0.65, and longer in winter (approximately 2.26 months) with an average r-value of 0.48 (Figure 10).

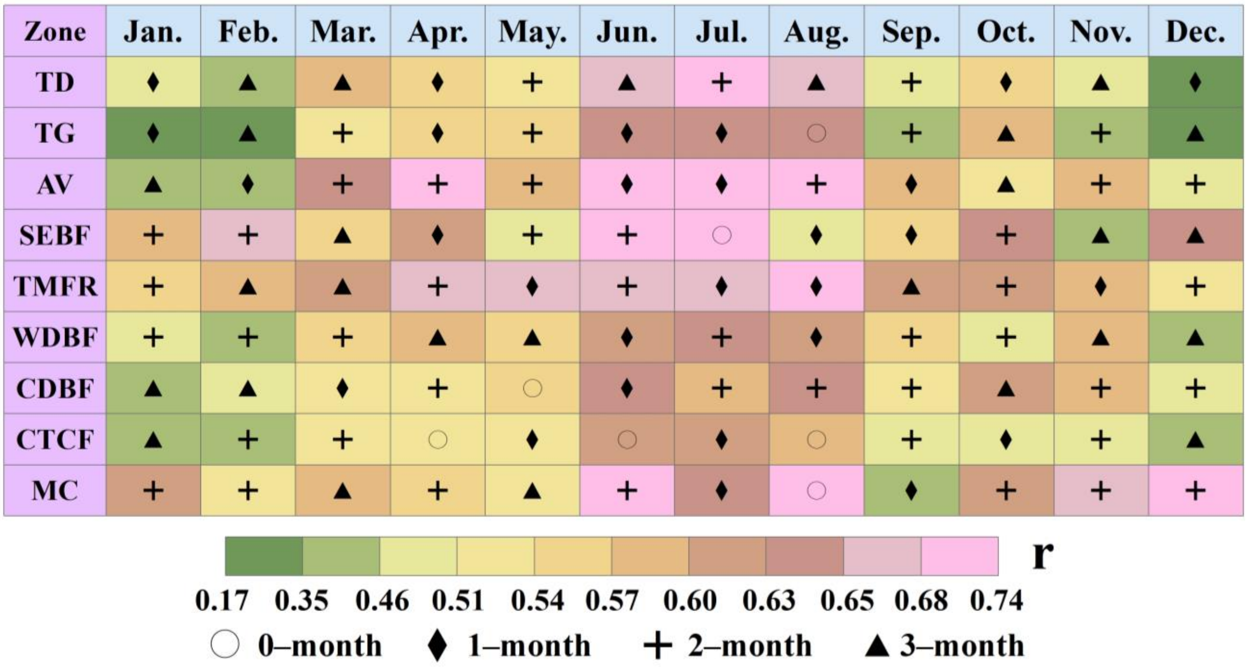

Figure 10. The propagation features from meteorological drought to vegetation drought across China. Green and pink colors indicate lower and higher r values.

5. Discussion

5.1. Dynamic Relations between Vegetation Drought and Atmospheric Teleconnection

5.1.1. Bivariate Wavelet Coherence

The bivariate wavelet coherence (BWC) and multivariate wavelet coherence (MWC) were used to reveal the dynamic relations between vegetation drought and atmospheric teleconnection across China. Figure 11 depicts the BWC-based internal relations between the monthly VCI and eight teleconnection data (ENSO, AO, SOI, PNA, SI, DMI, TPI, and NPI) during 1999–2020. There are four common periods with negative relations in VCI-ENSO (Figure 11a), with signals of 10–14 (2001–2002), 16–20 (2009–2010), 30–40 (2011–2013), and 10–14 months (2016–2018). There are two common periods with negative relations in VCI-AO (Figure 11b), with signals of 12–14 (2001–2002), and 10–14 months (2014–2015). Figure 11c indicates that VCI is negatively correlated with SOI with a signal of 10–16 months (2014–2017). Figure 11d shows that there are three common periods in VCI-PNA, which are 10–16 in 2000–2003 and 10–14 months in 2007–2008 with negative relations, and 10–16 months in 2012–2018 with positive relations. Meanwhile, the relations between VCI and the other four atmospheric teleconnections (SI, DMI, TPI, and NPI) are illustrated in Figure 11e–h. Furthermore, there is a short-term mutual period (1–8 months) between VCI and atmospheric teleconnection from 1999 to 2020. In general, the results show that PNA has the strongest influence on vegetation drought across China.

Also, we explored the common features between vegetation drought and atmospheric teleconnection within the low-energy areas based on the BWC (Figure 12). There are two obvious negative relations in VCI-ENSO (Figure 12a), with signals of 14–16 (2000–2001), and 14–20 months (2009–2010). There is an obvious positive relation in VCI-AO (Figure 12b), with a signal of 14–24 months (2007–2014), and two negative correlations with signals of 8–14 (2001–2003), and 8–12 months (2009–2010). There are two obvious positive relations in VCI-SOI (Figure 12c), with signals of 10–16 (2001–2004) and 8–12 months (2006–2007), and two negative relations with signals of 24–32 (2007–2010) and 8–14 months (2014–2017). Figure 12d indicates that VCI is positively correlated with PNA with a signal of 8–14 months (2001–2004), and negatively correlated with PNA with a signal of 48–96 months (2007–2014). In addition, there are obvious relations between vegetation drought and other atmospheric teleconnections (SI, DMI, TPI, and NPI) in both frequency and temporal domains (Figure 12e–h).

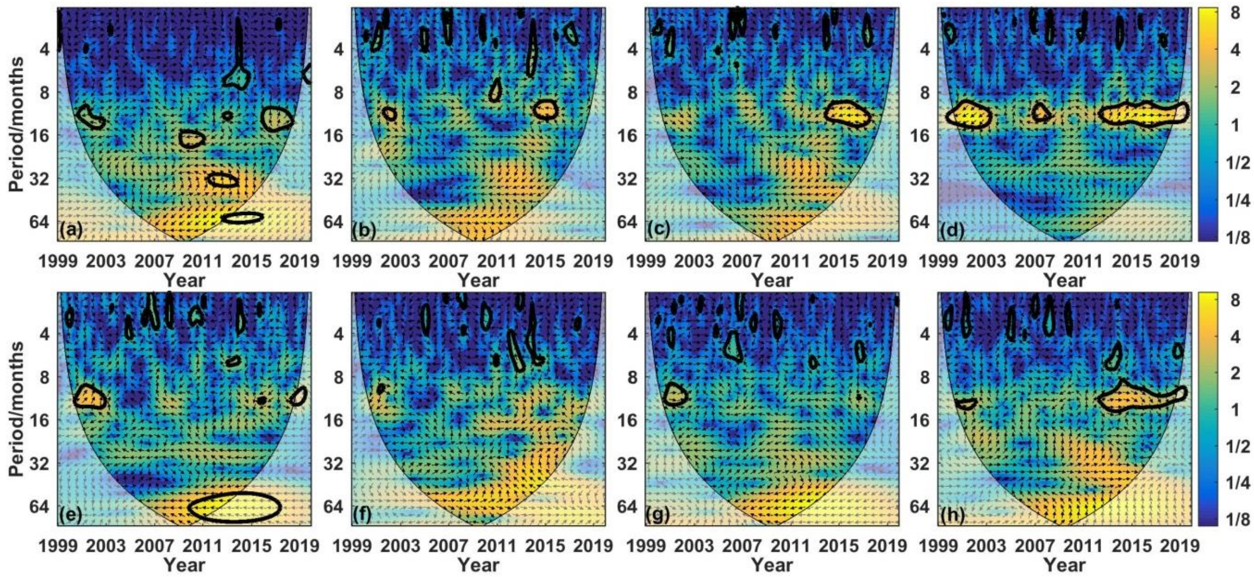

Figure 11. The relations between the monthly VCI and (**a**) ENSO, (**b**) AO, (**c**) SOI, (**d**) PNA, (**e**) SI, (**f**) DMI, (**g**) TPI, and (**h**) NPI data during 1999–2020 across China, respectively. The thick contour denotes a 95% confidence level. The colors in the legend indicate wavelet energy.

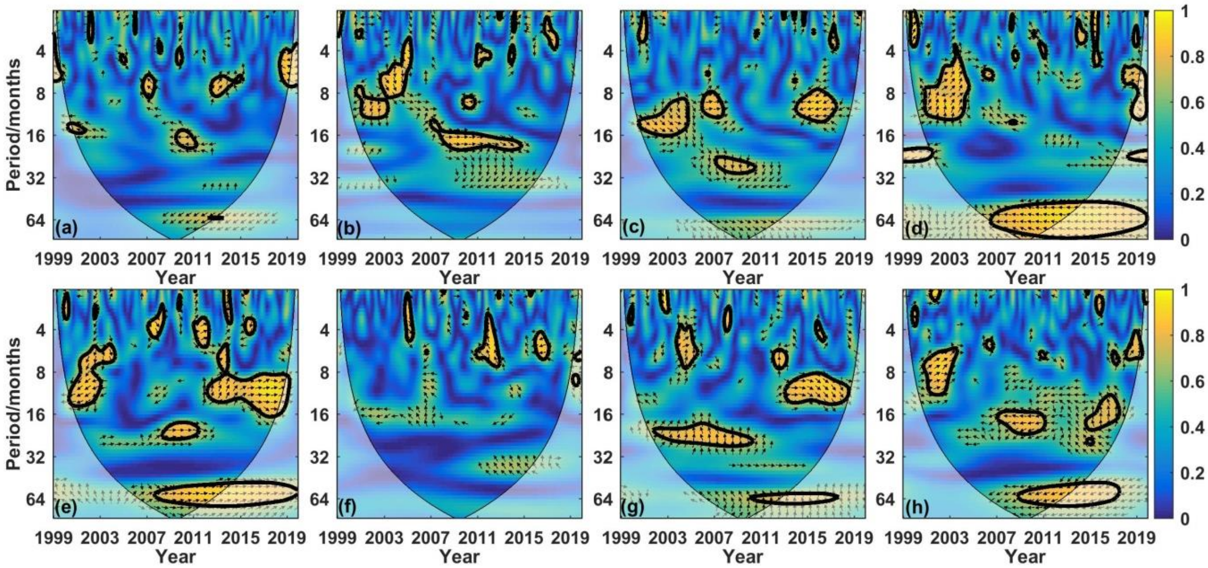

Figure 12. The BWC in VCI and (**a**) ENSO, (**b**) AO, (**c**) SOI, (**d**) PNA, (**e**) SI, (**f**) DMI, (**g**) TPI, and (**h**) NPI data during 1999–2020 across China, respectively. The thick contour denotes a 95% confidence level. The colors in the legend indicate wavelet energy.

5.1.2. Multivariate Wavelet Coherence

Since PNA has the most obvious impact on vegetation drought, we adopted MWC between VCI-PNA and other atmospheric teleconnections (ENSO, AO, SOI, SI, DMI, TPI, and NPI) to clarify the simultaneous influence of multiple atmospheric teleconnections on vegetation drought (Figure 13). VCI-PNA is closely related to ENSO (Figure 13a), with signals of 8–14 (2001–2003) and 24–96 months (2005–2016). There are three common periods in VCI-PNA-AO (Figure 13b), with signals of 8–14 (2001–2006), 48–96 (2010–2013), and 24–40 months (2011–2015). There are four common periods in VCI-PNA-SOI (Figure 13c), with signals of 8–14 (2000–2004), 8–14 (2005–2008), 48–96 (2005–2014), and 8–14 months (2013–2018). VCI-PNA is closely related to SI (Figure 13d), with signals of 8–12 (2001–2004), 48–64 (2009–2013), and 8–16 months (2012–2018). Meanwhile, the relations between VCI-PNA and the other three atmospheric teleconnections are depicted in Figure 13e–g. In general, the combination of PNA and ENSO has the strongest coupled effects on vegetation drought across China.

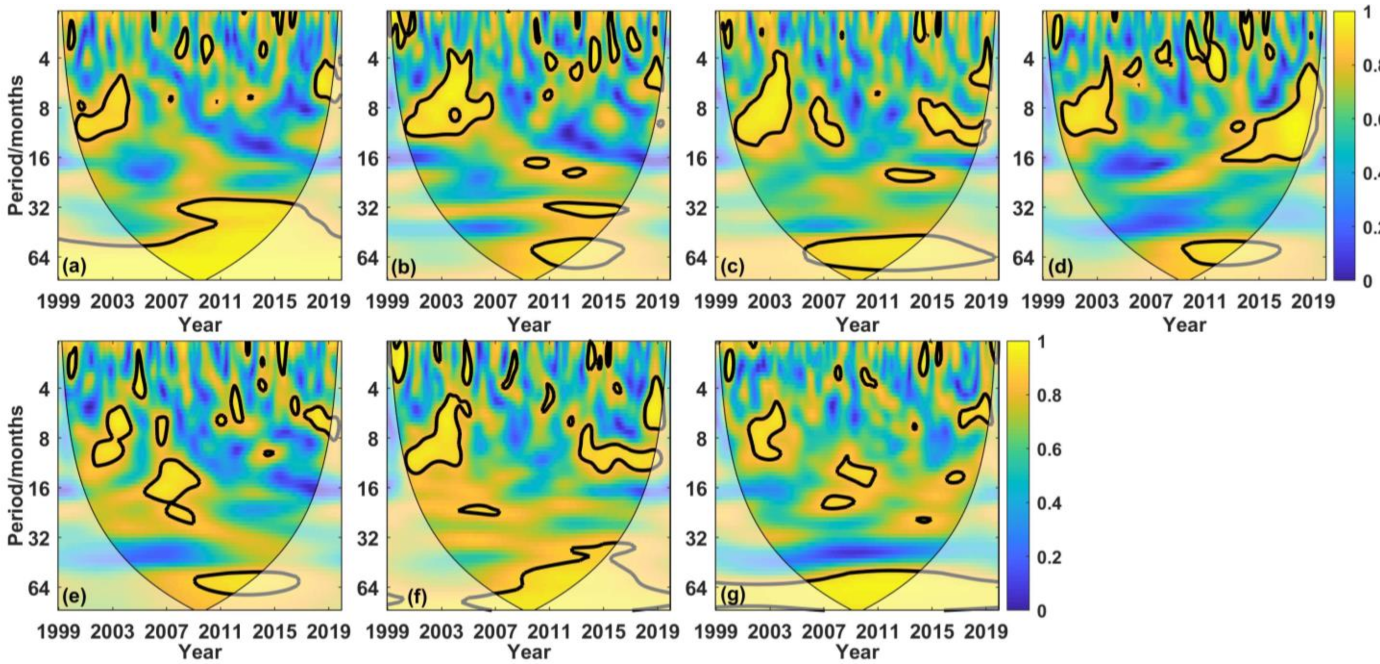

Figure 13. The MWC in VCI-PNA and (**a**) ENSO, (**b**) AO, (**c**) SOI, (**d**) SI, (**e**) DMI, (**f**) TPI, and (**g**) NPI data during 1999–2020 across China, respectively. The thick contour denotes a 95% confidence level. The colors in the legend indicate wavelet energy.

In view of the obvious impact of PNA and ENSO on vegetation drought, the relations between the VCI-PNA-ENSO and other atmospheric teleconnections (AO, SOI, SI, DMI, TPI, and NPI) were also explored (Figure 14). For one factor, PNA has the closest relation to vegetation drought, with an average wavelet coherence (AWC) of 0.81 and a percent area of significant coherence (PASC) of 16.04%. For two factors, PNA-ENSO has the most obvious effect on vegetation drought (AWC = 0.94, PASC = 25.60%). For three factors, PNA-ENSO-TPI has the strongest impact on vegetation drought (AWC = 0.98, PASC = 26.62%). When three factors are involved, the AWC and PASC values are no less than 0.97 and 20%, respectively (Table 4). Thus, the combination of three factors (PNA-ENSO-TPI) can elucidate the vegetation drought variations across China.

Table 4. The AWC and PASC between vegetation drought and atmospheric teleconnections.

One-Factor	AWC	PASC (%)	Two-Factors	AWC	PASC (%)	Three-Factors	AWC	PASC (%)
ENSO	0.77	3.79	PNA-ENSO	0.94	25.60	PNA-ENSO-AO	0.97	24.66
AO	0.78	6.18	PNA-AO	0.91	11.75	PNA-ENSO-SOI	0.98	25.38
SOI	0.78	6.17	PNA-SOI	0.92	15.10	PNA-ENSO-SI	0.97	23.04
PNA	0.81	16.04	PNA-SI	0.91	13.16	PNA-ENSO-DMI	0.97	21.79
SI	0.81	15.14	PNA-DMI	0.90	8.77	PNA-ENSO-TPI	0.98	26.62
DMI	0.77	2.22	PNA-TPI	0.93	17.62	PNA-ENSO-NPI	0.97	20.58
TPI	0.78	7.87	PNA-NPI	0.93	16.75			
NPI	0.79	9.43						

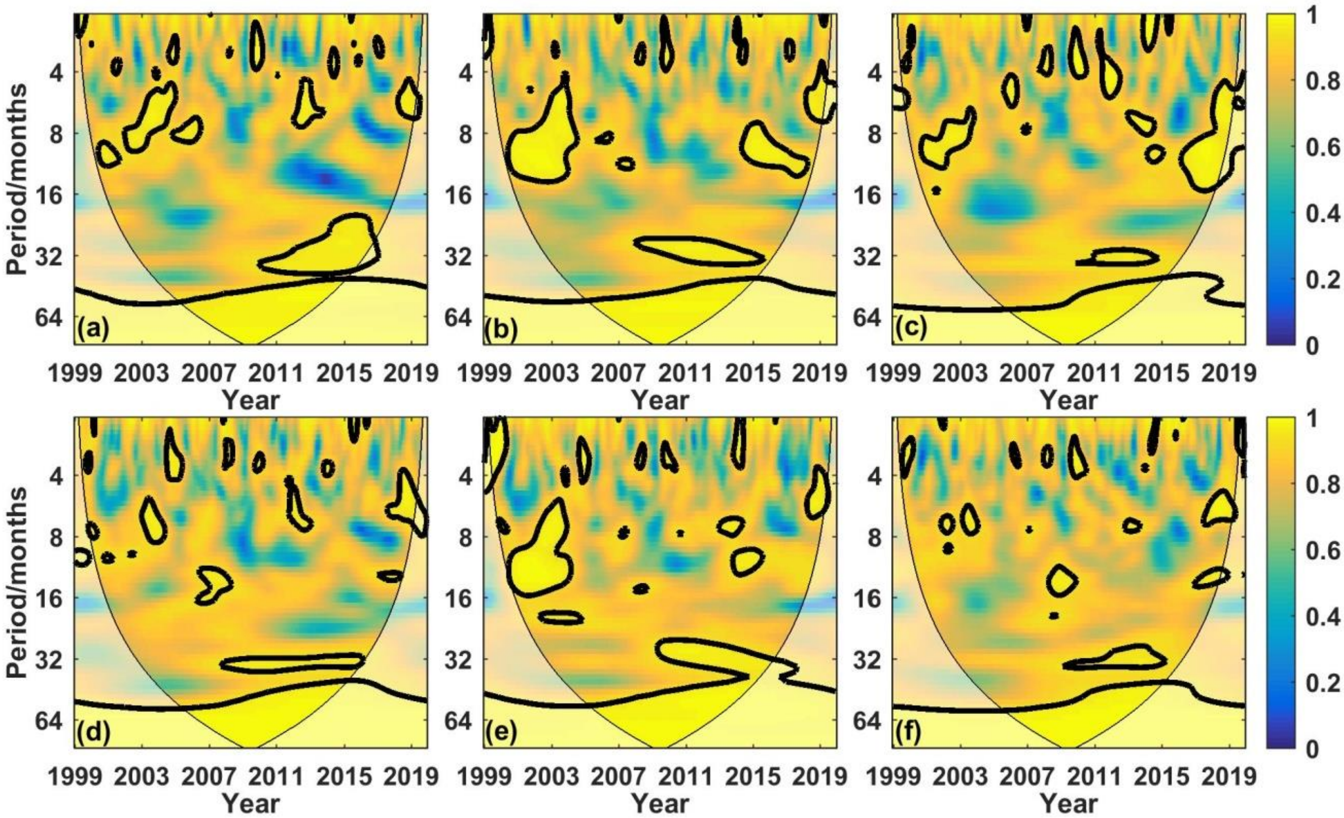

Figure 14. The MWC in VCI-PNA-ENSO and (**a**) AO, (**b**) SOI, (**c**) SI, (**d**) DMI, (**e**) TPI, and (**f**) NPI data during 1999–2020 across China, respectively. The thick contour denotes a 95% confidence level. The colors in the legend indicate wavelet energy.

5.2. Uncertainties

In this study, there are several aspects of uncertainty. For example, although some uncertainties may have occurred during the process of interpolating station-derived SPEI to different spatial resolutions, we obtained an SPEI dataset with the same resolution as the remote sensed-based vegetation dataset [51,58]. Another uncertainty was in the remote sensing datasets because of poor atmospheric conditions and cloud contamination, and it was a commonly existing phenomenon for satellite images [24,26,59]. Nonetheless, this problem may be diminished by filtering, re-processing, and de-noising. Additionally, while taking VCI to reflect vegetation greenness change, other indices are considered to be a better alternative, such as the vegetation health index (VHI), which can reflect vegetation growth status and land surface temperature [16,46]. Since it was still a non-deterministic work for quantifying and determining the weights of VHI components, we applied VCI to investigate the vegetation ecosystem responses to drought in an operational manner [15]. However, despite several uncertainties, our findings provided a reference for vegetation drought planning and management across China.

5.3. The Possible Influence Factors

The applicability of VCI was quantitatively evaluated from a different sensor, and the results indicated that it is suitable for identifying vegetation drought across China. Meanwhile, the consistency in the TD is lower than that in the TG and WDBF, which may be due to the scarcity of vegetation in the TD [60,61]. The increase in global temperature and the change in the precipitation pattern can accelerate the development progression of vegetation drought [29]. In China, the least annual precipitation occurs in the TD (213.10 mm), AV (363.34 mm) and CDBF (568.74 mm), while the lowest annual temperature occurs in the AV (4.11 °C), CDBF (4.17 °C) and TD (7.16 °C), resulting in relatively serious vegetation drought in these three regions. Specifically, the TD is located in the arid inland areas with desertification land, and the AV is located in the high-altitude areas with less precipitation, which may be the reason for the serious vegetation drought in these two areas [18,25]. As for the vegetation drought in the CDBF, it may be caused by monsoon climate, forest fires, and excessive deforestation [62]. In recent years, ecological management measures in the SEBF have resulted in an exuberant vegetation coverage on the originally bare land surface, and improved ecological and environmental health in this area [63,64]. Moreover, in addition to some direct impacts of climate change, the increase in crop planting has improved the multiple-crop index and grain yield, leading to the expanding agricultural cultivation scope, rising vegetation growth and descending vegetation drought trend [20,65]. In addition to meteorological conditions, anthropogenic factors (e.g., grain for green, tree planting, and afforestation) and topographic conditions will also affect the propagation process of drought [35,38,39]. Since the SPOT/VEGETATION satellite was launched in April 1998, the period 1999–2020 was selected to ensure the completeness of data in a natural year. In Figure 7, the trends without statistical significance may be associated with a relatively short cycle time.

Previous studies [41–43] have shown that drought is vulnerable to circumfluence index variation, and the relationship between drought and large-scale circumfluence factor has attracted widespread attention from decision makers. As one of the most obvious patterns of low-frequency variation, PNA is related to the intense fluctuations in the jet stream intensity [66,67]. ENSO is a wind field oscillation over the equatorial eastern Pacific and is regarded as an ocean–atmosphere interaction phenomenon and an important influence factor in climate prediction [2,54]. Furthermore, TPI is a significant climate variability with a basin scale, which has an obvious function in climate anomalies [68]. In this paper, it is recognized that the combination of PNA, ENSO, and TPI is most closely related to vegetation drought, which is new evidence that can explain vegetation drought variations across China (Figure 14). Therefore, PNA-ENSO-TPI, which affects vegetation drought, can be considered as the input factor for improving the prediction ability of vegetation drought.

5.4. Advantages and Limitations

In this study, VCI was adopted to reflect the ecological response capacity of vegetation under drought stress [16,17,59]. Due to the vast geographical scope and differentiated climatic patterns, the whole of China was classified into several large vegetation subzones [57]. Substantially, the rising vegetation drought was mainly distributed in the TD and AV. The trend item identified by ESMD can reflect the overall fluctuation characteristics of time series and has significant advantages in drought investigation [69]. As presented in Figure 4, the ESMD results also showed that the trend items were decreasing in the TD and AV, which was consistent with the pixel-scaled trend identification. Besides, consistent with the description in Figure 4, the SEBF was an area with the most obvious VCI upward trend. The pixel-scaled trend features showed that the vegetation drought was slowing down during 1999–2020, which could be concluded from the variations of vegetation drought in Section 4.2. The finding was consistent with other studies [19,20,64,65], which investigated vegetation growth conditions in each sub-region of China.

In addition, the lag-time characteristics between meteorological drought and vegetation drought can help us predict the occurrence of vegetation drought, with great significance for maintaining a benign cycle in the ecosystem, promoting harmonious development of ecology and economy, and optimizing the ecological environment. Similarly, some researchers [36,70] have found that the propagation dynamics were non-linear and time-variant. The discovery of complex and different propagation relationships also supported this result. Meanwhile, the propagation time had seasonal characteristics and spatial differences (Figure 10). Ding et al. reported a stronger drought transmission in summer ($r = 0.5$–0.7), which was similar to the results of the present study [57].

In terms of limitations, given the availability of remote sensing products, only the data for the past 22 years were adopted. Moreover, limited by the lack of observation data on ecological vegetation growth and water consumption, it is also a future development tendency to propose a comprehensive vegetation drought index reflecting meteorological, hydrological, and ecological vegetation information based on multi-source remote sensing inversion data [4].

6. Conclusions

In this study, the spatial–temporal evolution of vegetation drought and their relationships with atmospheric teleconnection were analyzed during 1999–2020. Additionally, the propagation characteristics were explored between vegetation drought and meteorological drought. According to the analysis results, the major conclusions of the study are:

(1) In 1999–2020, the vegetation drought presented an overall decreasing trend, while the performance was different in each subzone. Noticeably, the minimal VCI-value (0.41) was found in 2000, and the average monthly VCI was 0.36–0.46.
(2) From spring to winter, the worst vegetation drought with minimal VCI-values appeared in the AV (0.47), AV (0.45), CTCF (0.49), and CDBF (0.38), respectively. Additionally, the three vegetation-drought-prone areas in China were the CDBF, CTCF and AV.
(3) The pixel-scaled drought trend identification indicated that vegetation droughts were increasing in January and February and were decreasing from March to December on a monthly scale. On a seasonal scale, vegetation droughts were alleviating in each season across China.
(4) The influence of atmospheric teleconnection on the formation of drought cannot be ignored. The results showed that PNA-ENSO-TPI had the strongest effects on the vegetation drought evolution process.

Author Contributions: Conceptualization, S.G. and F.W.; Methodology, H.L. (Hexin Lai) and D.D.; original draft preparation, S.G.; funding acquisition, X.Q. and H.L. (Hao Li). All authors have read and agreed to the published version of the manuscript.

Funding: This research was supported by the China Postdoctoral Science Foundation (2022M722879), Henan Province Science and Technology Research Project (232102321014), Basic Scientific Research Project of the Chinese Academy of Agricultural Sciences (Grant No. FIRI2021010601), Key Technologies R&D and Promotion Program of Henan Province (Grant No. 212102110031), High-Levelevel Talent Research Initiation Project, North China University of Water Resources and Electric Power (grant number 202004004).

Data Availability Statement: Data can be requested from the corresponding author upon reasonable request.

Acknowledgments: Thanks for the help with language editing provided by Zezhong Zhang.

Conflicts of Interest: The authors declare no conflict of interest.

References

1. Mishra, A.K.; Singh, V.P. A review of drought concepts. *J. Hydrol.* **2010**, *391*, 202–216. [CrossRef]
2. Forootan, E.; Khaki, M.; Schumacher, M.; Wulfmeyer, V.; Mehrnegar, N.; van Dijk, A.I.J.M.; Brocca, L.; Farzaneh, S.; Akinluyi, F.; Ramillien, G.; et al. Understanding the global hydrological droughts of 2003–2016 and their relationships with teleconnections. *Sci. Total Environ.* **2019**, *650*, 2587–2604. [CrossRef]
3. Mehdizadeh, S.; Ahmadi, F.; Mehr, A.D.; Safari, M.J.S. Drought modeling using classic time series and hybrid wavelet-gene expression programming models. *J. Hydrol.* **2020**, *587*, 125017.
4. Jiang, T.L.; Su, X.L.; Singh, V.P.; Zhang, G.X. A novel index for ecological drought monitoring based on ecological water deficit. *Ecol. Indic.* **2021**, *129*, 107804. [CrossRef]
5. Crausbay, S.D.; Ramirez, A.R.; Carter, S.L.; Cross, M.S.; Hall, K.R.; Bathke, D.J.; Betancourt, J.L.; Colt, S.; Cravens, A.E.; Dalton, M.S.; et al. Defining ecological drought for the twenty-first century. *Bull. Am. Meteorol. Soc.* **2017**, *98*, 2543–2550. [CrossRef]
6. Wu, D.; Qu, J.J.; Hao, X.J. Agricultural drought monitoring using MODIS-based drought indices over the USA Corn Belt. *Int. J. Remote Sens.* **2015**, *36*, 5403–5425. [CrossRef]
7. Wang, Y.J.; Fu, B.J.; Liu, Y.X.; Li, Y.; Feng, X.M.; Wang, S. Response of vegetation to drought in the Tibetan Plateau: Elevation differentiation and the dominant factors. *Agric. Forest Meteorol.* **2021**, *306*, 108468.

8. Caccamo, G.; Chisholm, L.A.; Bradstock, R.A.; Puotinen, M.L. Assessing the sensitivity of MODIS to monitor drought in high biomass ecosystems. *Remote Sens. Environ.* **2011**, *115*, 2626–2639. [CrossRef]
9. Kuri, F.; Murwira, A.; Murwira, K.S.; Masocha, M. Predicting maize yield in Zimbabwe using dry dekads derived from remotely sensed Vegetation Condition Index. *Int. J. Appl. Earth Obs.* **2014**, *33*, 39–46.
10. Zambrano, F.; Lillo-Saavedra, M.; Verbist, K.; Lagos, O. Sixteen years of agricultural drought assessment of the BioBío region in Chile using a 250 m resolution vegetation condition index (VCI). *Remote Sens.* **2016**, *8*, 530.
11. Agutu, N.O.; Awange, J.L.; Zerihun, A.; Ndehedehe, C.E.; Kuhn, M.; Fukuda, Y. Assessing multi-satellite remote sensing, reanalysis, and land surface models' products in characterizing agricultural drought in East Africa. *Remote Sens. Environ.* **2017**, *194*, 287–302.
12. Zhao, A.Z.; Zhang, A.B.; Liu, J.H.; Feng, L.L.; Zhao, Y.L. Assessing the effects of drought and "Grain for Green" Program on vegetation dynamics in China's Loess Plateau from 2000 to 2014. *Catena* **2019**, *175*, 446–455.
13. McEvoy, J.; Bathke, D.J.; Burkardt, N.; Cravens, A.E.; Haigh, T.; Hall, K.R.; Hayes, M.J.; Jedd, T.; Podêbradská, M.; Wickham, E. Ecological drought: Accounting for the non-human impacts of water shortage in the upper Missouri headwaters basin, Montana, USA. *Resources* **2018**, *7*, 14.
14. Duo, A.; Zhao, W.J.; Qu, X.Y.; Jing, R.; Xiong, K. Spatio-temporal variation of vegetation coverage and its response to climate change in North China plain in the last 33 years. *Int. J. Appl. Earth Obs.* **2016**, *53*, 103–117.
15. Bento, V.A.; Gouveia, C.M.; DaCamara, C.C.; Trigo, I.F. A climatological assessment of drought impact on vegetation health index. *Agric. Forest Meteorol.* **2018**, *259*, 286–295. [CrossRef]
16. Xie, F.; Fan, H. Deriving drought indices from MODIS vegetation indices (NDVI/EVI) and Land Surface Temperature (LST): Is data reconstruction necessary? *Int. J. Appl. Earth Obs.* **2021**, *101*, 102352.
17. Quiring, S.M.; Ganesh, S. Evaluating the utility of the Vegetation Condition Index (VCI) for monitoring meteorological drought in Texas. *Agric. Forest Meteorol.* **2010**, *150*, 330–339.
18. Shao, Y.Y.; Zhang, Y.Q.; Wu, X.Q.; Bourque, P.A.; Zhang, J.T.; Qin, S.G.; Wu, B. Relating historical vegetation cover to aridity patterns in the greater desert region of northern China: Implications to planned and existing restoration projects. *Ecol. Indic.* **2018**, *89*, 528–537.
19. Jiang, W.G.; Yuan, L.H.; Wang, W.J.; Cao, R.; Zhang, Y.F.; Shen, W.M. Spatio-temporal analysis of vegetation variation in the Yellow River Basin. *Ecol. Indic.* **2015**, *51*, 117–126.
20. Zhao, J.; Huang, S.Z.; Huang, Q.; Wang, H.; Leng, G.Y.; Fang, W. Time-lagged response of vegetation dynamics to climatic and teleconnection factors. *Catena* **2020**, *189*, 104474.
21. Kou, P.L.; Xu, Q.; Jin, Z.; Yunus, A.P.; Luo, X.B.; Liu, M.H. Complex anthropogenic interaction on vegetation greening in the Chinese Loess Plateau. *Sci. Total Environ.* **2021**, *778*, 146065. [CrossRef]
22. Carter, G.A. Responses of leaf spectral reflectance to plant stress. *Am. J. Bot.* **1993**, *80*, 239–243. [CrossRef]
23. Lin, Q.X.; Wu, Z.Y.; Singh, V.P.; Sadeghi, S.H.R.; He, H.; Lu, G.H. Correlation between hydrological drought, climatic factors, reservoir operation, and vegetation cover in the Xijiang Basin, South China. *J. Hydrol.* **2017**, *549*, 512–524.
24. Mo, K.L.; Chen, Q.W.; Chen, C.; Zhang, J.Y.; Wang, L.; Bao, Z.X. Spatiotemporal variation of correlation between vegetation cover and precipitation in an arid mountain-oasis river basin in northwest China. *J. Hydrol.* **2019**, *574*, 138–147.
25. Fan, Z.M.; Bai, X.Y. Scenarios of potential vegetation distribution in the different gradient zones of Qinghai-Tibet Plateau under future climate change. *Sci. Total Environ.* **2021**, *796*, 148918. [PubMed]
26. Huang, W.H.; Wang, H.L. Drought and intensified agriculture enhanced vegetation growth in the central Pearl River Basin of China. *Agr. Water Manag.* **2021**, *256*, 107077.
27. Venkataraman, K.; Tummuri, S.; Medina, A.; Perry, J. 21st century drought outlook for major climate divisions of Texas based on CMIP5 multimodel ensemble: Implications for water resource management. *J. Hydrol.* **2016**, *534*, 300–316.
28. John, F.; Toth, R.; Frank, K.; Groeneveld, J.; Müller, B. Ecological vulnerability through insurance? Potential unintended consequences of livestock drought insurance. *Ecol. Econ.* **2019**, *157*, 357–368.
29. Crausbay, S.D.; Betancourt, J.; Bradford, J.; Cartwright, J.; Dennison, W.C.; Dunham, J.; Enquist, C.A.F.; Frazier, A.G.; Hall, K.R.; Littell, J.S.; et al. Unfamiliar territory: Emerging themes for ecological drought research and management. *One Earth* **2020**, *3*, 337–353.
30. Park, S.Y.; Sur, C.Y.; Lee, J.H.; Kim, J.S. Ecological drought monitoring through fish habitat-based flow assessment in the Gam river basin of Korea. *Ecol. Indic.* **2020**, *109*, 105830.
31. Millar, C.I.; Stephenson, N.L. Temperate forest health in an era of emerging megadisturbance. *Science* **2015**, *349*, 823–826. [CrossRef] [PubMed]
32. Deng, S.F.; Yang, T.B.; Zeng, B.; Zhu, X.F.; Xu, H.J. Vegetation cover variation in the Qilian Mountains and its response to climate change in 2000–2011. *J. Mt. Sci.* **2013**, *10*, 1050–1062.
33. Guo, W.W.; Huang, S.Z.; Huang, Q.; Leng, G.Y.; Mu, Z.X.; Han, Z.M.; Wei, X.T.; She, D.X.; Wang, H.Y.; Wang, Z.X.; et al. Drought trigger thresholds for different levels of vegetation loss in China and their dynamics. *Agric. Forest Meteorol.* **2023**, *331*, 109349. [CrossRef]
34. Zhang, Y.; Hao, Z.C.; Feng, S.F.; Zhang, X.; Xu, Y.; Hao, F.H. Agricultural drought prediction in China based on drought propagation and large-scale drivers. *Agric. Water Manag.* **2021**, *255*, 107028.

35. Bae, H.; Ji, H.; Lim, Y.J.; Ryu, Y.; Kim, M.H.; Kim, B.J. Characteristics of drought propagation in South Korea: Relationship between meteorological, agricultural, and hydrological droughts. *Nat. Hazards* **2019**, *99*, 1–16.
36. Wu, J.W.; Miao, C.Y.; Zheng, H.Y.; Duan, Q.Y.; Lei, X.H.; Li, H. Meteorological and hydrological drought on the Loess Plateau, China: Evolutionary characteristics, impact, and propagation. *J. Geophys. Res. Atmos.* **2018**, *123*, 11569–11584.
37. Wang, F.; Wang, Z.M.; Yang, H.B.; Di, D.Y.; Zhao, Y.; Liang, Q.H. Utilizing GRACE-based groundwater drought index for drought characterization and teleconnection factors analysis in the North China Plain. *J. Hydrol.* **2020**, *585*, 124849.
38. Huang, S.Z.; Li, P.; Huang, Q.; Leng, G.Y.; Hou, B.B.; Ma, L. The propagation from meteorological to hydrological drought and its potential influence factors. *J. Hydrol.* **2017**, *547*, 184–195. [CrossRef]
39. Xu, Y.; Zhang, X.; Wang, X.; Hao, Z.C.; Singh, V.P.; Hao, F.H. Propagation from meteorological drought to hydrological drought under the impact of human activities: A case study in northern China. *J. Hydrol.* **2019**, *579*, 124147.
40. Huang, S.Z.; Huang, Q.; Chang, J.X.; Leng, G.Y.; Xing, L. The response of agricultural drought to meteorological drought and the influencing factors: A case study in the Wei River Basin, China. *Agric. Water Manag.* **2015**, *159*, 45–54.
41. Manzano, A.; Clemente, M.A.; Morata, A.; Luna, M.Y.; Beguería, S.; Vicente-Serrano, S.M.; Martín, M.L. Analysis of the atmospheric circulation pattern effects over SPEI drought index in Spain. *Atmos. Res.* **2019**, *230*, 104630.
42. Vazifehkhah, S.; Kahya, E. Hydrological and agricultural droughts assessment in a semi-arid basin: Inspecting the teleconnections of climate indices on a catchment scale. *Agric. Water Manag.* **2019**, *217*, 413–425.
43. Cheng, Q.P.; Gao, L.; Zhong, F.L.; Zuo, X.A.; Ma, M.M. Spatiotemporal variations of drought in the Yunnan-Guizhou Plateau, southwest China, during 1960–2013 and their association with large-scale circulations and historical records. *Ecol. Indic.* **2020**, *112*, 106041.
44. Cardil, A.; Rodrigues, M.; Ramirez, J.; de-Miguel, S.; Silva, C.A.; Mariani, M.; Ascoli, D. Coupled effects of climate teleconnections on drought, Santa Ana winds and wildfires in southern California. *Sci. Total Environ.* **2021**, *765*, 142788.
45. Ning, T.T.; Liu, W.Z.; Lin, W.; Song, X.Q. NDVI variation and its responses to climate change on the Northern Loess Plateau of China from 1998 to 2012. *Adv. Meteorol.* **2015**, *2015*, 725427.
46. Bento, V.A.; Gouveia, C.M.; DaCamara, C.C.; Libonati, R.; Trigo, I.F. The roles of NDVI and Land Surface Temperature when using the Vegetation Health Index over dry regions. *Global Planet. Change* **2020**, *190*, 103198.
47. Holben, B.N. Characteristics of maximum-value composite images from temporal AVHRR data. *Int. J. Remote Sens.* **1986**, *7*, 1417–1434.
48. Blumberg, D.G. Analysis of large aeolian (wind-blown) bedforms using the Shuttle Radar Topography Mission (SRTM) digital elevation data. *Remote Sens. Environ.* **2006**, *100*, 179–189.
49. Wang, C.L.; Jiang, Q.O.; Shao, Y.Q.; Sun, S.Y.; Xiao, L.; Guo, J.B. Ecological environment assessment based on land use simulation: A case study in the Heihe River Basin. *Sci. Total Environ.* **2019**, *697*, 133928.
50. Vicente-Serrano, S.M.; Beguería, S.; López-Moreno, J.I. A multiscalar drought index sensitive to global warming: The Standardized Precipitation Evapotranspiration Index. *J. Clim.* **2010**, *23*, 1696–1718.
51. Tong, S.Q.; Lai, Q.; Zhang, J.Q.; Bao, Y.H.; Lusi, A.; Ma, Q.Y.; Li, X.Q.; Zhang, F. Spatiotemporal drought variability on the Mongolian Plateau from 1980–2014 based on the SPEI-PM, intensity analysis and Hurst exponent. *Sci. Total Environ.* **2018**, *615*, 1557–1565.
52. Wang, J.L.; Li, Z.J. Extreme-point symmetric mode decomposition method for data analysis. *Adv. Adapt. Data Anal.* **2013**, *5*, 1350015. [CrossRef]
53. Hurst, H.E. Long term storage capacity of reservoirs. *Trans. Am. Soc. Civ. Eng.* **1951**, *116*, 776–808.
54. Nalley, D.; Adamowski, J.; Biswas, A.; Gharabaghi, B.; Hu, W. A multiscale and multivariate analysis of precipitation and streamflow variability in relation to ENSO, NAO and PDO. *J. Hydrol.* **2019**, *574*, 288–307.
55. Su, L.; Miao, C.Y.; Duan, Q.Y.; Lei, X.H.; Li, H. Multiple-wavelet coherence of world's large rivers with meteorological factors and ocean signals. *J. Geophys. Res. Atmos.* **2019**, *124*, 4932–4954.
56. Cheng, Q.P.; Zhong, F.L.; Wang, P. Potential linkages of extreme climate events with vegetation and large-scale circulation indices in an endorheic river basin in northwest China. *Atmos. Res.* **2021**, *247*, 105256.
57. Zhou, Z.Q.; Ding, Y.B.; Shi, H.Y.; Cai, H.J.; Fu, Q.; Liu, S.N.; Li, T.X. Analysis and prediction of vegetation dynamic changes in China: Past, present and future. *Ecol. Indic.* **2020**, *117*, 106642.
58. Angearu, C.V.; Ontel, I.; Boldeanu, G.; Mihailescu, D.; Nertan, A.; Craciunescu, V.; Catana, S.; Irimescu, A. Multi-temporal analysis and trends of the drought based on MODIS data in agricultural areas, Romania. *Remote Sens.* **2020**, *12*, 3940.
59. Zhong, S.B.; Sun, Z.H.; Di, L.P. Characteristics of vegetation response to drought in the CONUS based on long-term remote sensing and meteorological data. *Ecol. Indic.* **2021**, *127*, 107767.
60. Wang, N.; Guo, Y.C.; Wei, X.; Zhou, M.T.; Wang, H.J.; Bai, Y.B. UAV-based remote sensing using visible and multispectral indices for the estimation of vegetation cover in an oasis of a desert. *Ecol. Indic.* **2022**, *141*, 109155.
61. Zhou, D.C.; Zhang, L.X.; Hao, L.; Sun, G.; Xiao, J.F.; Li, X. Large discrepancies among remote sensing indices for characterizing vegetation growth dynamics in Nepal. *Agric. Forest. Meteorol.* **2023**, *339*, 109546.
62. Zhou, Z.Q.; Shi, H.Y.; Fu, Q.; Li, T.X.; Gan, T.Y.; Liu, S.N.; Liu, K. Is the cold region in Northeast China still getting warmer under climate change impact? *Atmos. Res.* **2020**, *237*, 104864.
63. Zhang, B.Q.; Wu, P.T.; Zhao, X.N.; Wang, Y.B.; Wang, J.W.; Shi, Y.G. Drought variation trends in different subregions of the Chinese Loess Plateau over the past four decades. *Agric. Water Manag.* **2012**, *115*, 167–177.

64. Naeem, S.; Zhang, Y.Q.; Zhang, X.Z.; Tian, J.; Abbas, S.; Luo, L.L.; Meresa, H.K. Both climate and socioeconomic drivers contribute to vegetation greening of the Loess Plateau. *Sci. Bull.* **2021**, *66*, 1160–1163.
65. Ma, F.Y.; Chen, J.Q.; Chen, J.S.; Wang, T.; Han, L.W.; Zhang, X.; Yan, J.H. Evolution of the hydro-ecological environment and its natural and anthropogenic causes during 1985–2019 in the Nenjiang River basin. *Sci. Total Environ.* **2021**, *799*, 149256.
66. Barnston, A.G.; Livezey, R.E. Classification, seasonality and persistence of low-frequency atmospheric circulation patterns. *Mon. Wea. Rev.* **1987**, *115*, 1083–1126.
67. Kenawy, A.M.; Buloshi, A.A.; Awadhi, T.A.; Nasiri, N.A.; Navarro-Serrano, F.; Alhatrushi, S.; Robaa, S.M.; Domínguez-Castro, F.; McCabe, M.F.; Schuwerack, P.M.; et al. Evidence for intensification of meteorological droughts in Oman over the past four decades. *Atmos. Res.* **2020**, *246*, 105126.
68. Enfield, D.B.; Mestas-Nunez, A.M.; Trimble, P.J. The Atlantic multidecadal oscillation and its relation to rainfall and river flows in the continental U.S. *Geophys. Res. Lett.* **2001**, *28*, 2077–2080.
69. Feng, K.; Su, X.L. Spatiotemporal characteristics of drought in the Heihe River Basin based on the extreme-point symmetric mode decomposition method. *Int. J. Disast. Risk Sc.* **2019**, *10*, 591–603.
70. Leng, G.Y.; Tang, Q.H.; Rayburg, S. Climate change impacts on meteorological, agricultural and hydrological droughts in China. *Global Planet. Change* **2015**, *126*, 23–34.